Eddy response to Southern Ocean climate modes

R. Morrow,[1] Marshall L. Ward,[2] Andrew McC. Hogg,[2] and S. Pasquet[1]

Received 9 October 2009; revised 12 April 2010; accepted 22 June 2010; published 13 October 2010.

[1] Interannual variations in Southern Ocean eddy kinetic energy (EKE) are investigated using 16 years of altimetric data. Circumpolar averages show a peak in EKE from 2000 to 2002, 2–3 years after the peak in the Southern Annular Mode (SAM) index. Although the SAM forcing is in phase around the circumpolar band, we find the EKE response varies regionally. The strongest EKE is in the Pacific, with energy peaks occurring progressively later toward the east. We suggest that this is due to the presence of two climate modes: SAM and ENSO. When strong positive SAM events coincide with La Niña periods, as in 1999, anomalous meridional wind forcing is enhanced in the South Pacific Ocean, contributing to the observed increase in EKE 2–3 years later. When positive SAM events coincide with El Niño periods, as in 1993, the climate modes are in opposition in the South Pacific, leading to a weak EKE response during the mid-1990s. Numerical modeling supports these observations. By applying different combinations of SAM and ENSO, we can reproduce both the elevated Pacific EKE response to SAM as well as an additional amplification/suppression of EKE during La Niña/El Niño. In general, we find that the EKE response depends on the interplay between wind forcing, topography, and mean flow and produces a strongly heterogeneous distribution in the Southern Ocean.

Citation: Morrow, R., M. L. Ward, A. M. Hogg, and S. Pasquet (2010), Eddy response to Southern Ocean climate modes, *J. Geophys. Res.*, *115*, C10030, doi:10.1029/2009JC005894.

1. Introduction

[2] Eddy processes play an important role in the dynamics and thermodynamics of the Southern Ocean. Strong air-sea heat and freshwater fluxes in the Southern Ocean, along with strong westerly winds, drive the deep-reaching eastward flowing Antarctic Circumpolar Current (ACC) as well as a vigorous meridional overturning circulation (MOC). Eddy fluxes, created by baroclinic and barotropic instabilities of this flow, act to maintain the balance of the ACC system. The eddy interfacial form stress helps transfer wind-driven momentum from the surface to the deep ocean layers where it is balanced by topographic form drag [*Munk and Palmén*, 1951; *Johnson and Bryden*, 1989]. In the absence of strong meridional currents in the upper ocean at these latitudes, eddies are also the principal mechanism for transferring heat, salt, and carbon poleward across the zonal ACC and contribute to the mixing of water masses through the diffusion of these tracers [*Sallée et al.*, 2008b]. Recent modeling studies have also shown how eddy fluxes act to maintain the strong meridional gradients of the ACC and contribute to the net transport of the MOC [*Treguier et al.*, 2007].

[3] Most of these eddy budget studies concentrate on mean statistics, but the Southern Ocean eddy field also evolves over time. Recently, *Hogg and Blundell* [2006], hereafter HB06, used a three-layer high-resolution quasi-geostrophic channel model with realistic topography to simulate the Southern Ocean's response to wind forcing. Their simple model produced intrinsic interannual variability under constant wind forcing, characterized by a large-scale increase in potential energy, followed by an increase in eddy kinetic energy (EKE) that peaked 2–3 years later. The model is in a "saturated" state, i.e., the model transport remains relatively stable, and the increased potential energy is transferred to the eddy field. The delay in EKE was caused by a positive feedback in the model; the increased potential energy creates favorable conditions for baroclinic instability, which increases eddy activity and the eddy momentum transfer to deeper layers. There interaction with the bottom topography induces a stronger meridional deep circulation which is intrinsically more unstable, increasing in turn the EKE. This feedback continues until the excess of large-scale potential energy is consumed.

[4] A corollary to the intrinsic variability of HB06 is that increases in wind stress have the potential to amplify the natural modes of variability. Such an increase in westerly wind forcing occurs during positive phases of the Southern Annular Mode (SAM). The Southern Annular Mode is the dominant climate mode in the Southern Hemisphere [*Thompson and Wallace*, 2000]. During its positive phase, there is an intensification of the midlatitude high-pressure band and the polar lows, leading to a near-annular meridional pressure difference (Figure 1a), which drives strong westerly wind anomalies, which are also shifted southward. Although there is a trend toward more positive SAM events over the last few decades, SAM also has high-frequency variations and strong

[1]LEGOS/CNRS, Toulouse, France.
[2]Research School of Earth Sciences, Australian National University, Canberra ACT, Australia.

0148-0227/10/2009JC005894

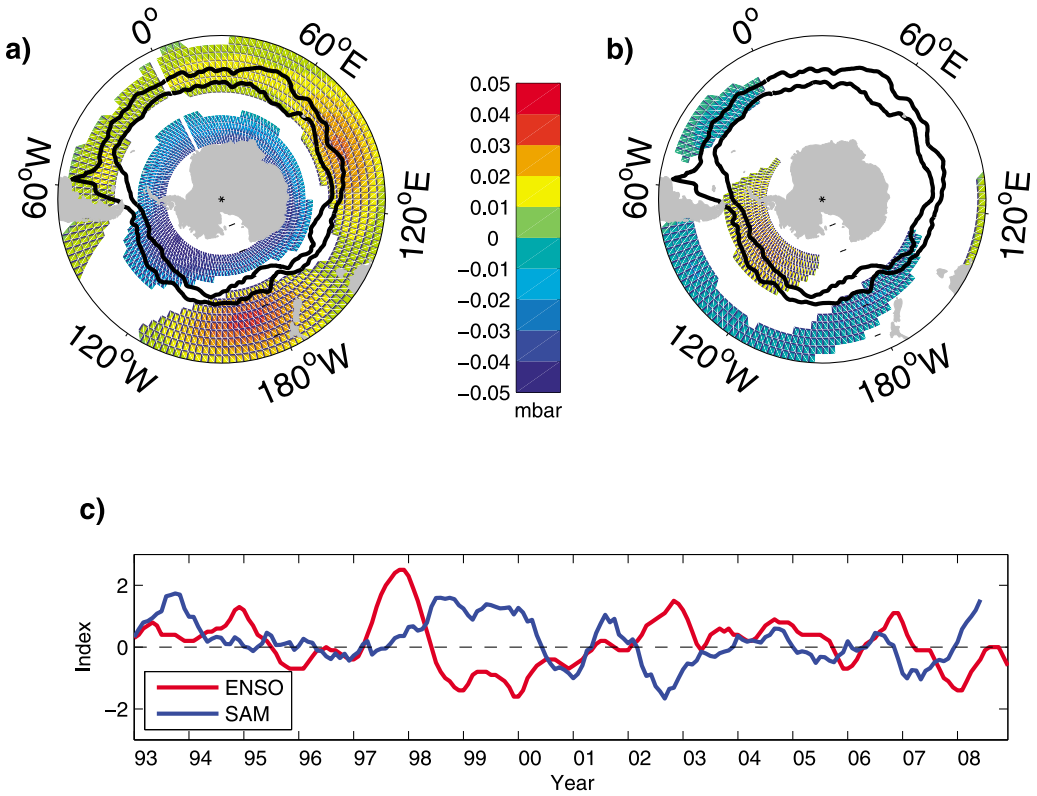

Figure 1. Regression of (a) SAM and (b) ENSO indices onto sea level pressure in the Southern Ocean. Black contours show the mean SAF and PF positions, after *Sallée et al.* [2008a]. (c) Temporal evolution of the SAM and ENSO indices from 1990–2007.

interannual variations. During the 1990s, strong positive SAM events occurred in 1993 and in 1998–1999 (Figure 1c).

[5] A second mode of climate variability in the Southern Hemisphere is associated with the El Niño Southern Oscillation (ENSO). Although this mode has tropical origins, it generates atmospheric Rossby waves, which propagate its signal to higher latitudes [*Karoly*, 1989], creating a dipole response in the South Pacific (Figure 1b), which induces local changes in the winds, sea surface temperature, and sea ice extent [*Stammerjohn et al.*, 2008]. Positive ENSO patterns are associated with El Niño events, strongest in 1997/1998, whereas negative ENSO is associated with La Niña events, strongest in 1999/2000 (Figure 1c).

[6] *Meredith and Hogg* [2006] (hereafter, MH06) have validated the 2–3 year delay found by the HB06 model by comparing the annual SAM index with basin-scale annual averages of EKE derived from satellite altimetry in the Atlantic, Indian, and Pacific sectors of the Southern Ocean. They indeed find an increase in observed EKE 2–3 years after the large peak in SAM in 1998/1999. In this paper, we extend their analysis to consider whether this large-scale EKE response occurs at the same time in all regions or whether there is a local response in relation to the two main climate modes, SAM and ENSO.

2. Data

2.1. EKE

[7] Altimetric EKE is calculated from weekly gridded sea level anomaly fields, issued by AVISO (http://www.aviso.oceanobs.com/fr/données/produits/index.html.), for the 14 year period January 1993 to December 2008. These data are on a Mercator grid, with 1/3° resolution in longitude, and variable resolution in latitude, from 1/4° at 30°S to 1/20° at 80°S. We use the DT-MSLA "Ref" series: homogeneous data sets based on two satellite missions (Topex/Poseidon/ERS or Jason-1/Envisat or Jason-2/Envisat) with the same ground track, assuring that the sampling is stable in time. Note that from January 1994 to March 1995, ERS was on a 185 day geodetic repeat, and only Topex-Poseidon data were available. This leads to a 30% decrease in EKE [*Ducet et al.*, 2000]. We prefer to have this small gap with lower resolution, rather than use T/P alone (as in MH06), which would lead to a 30% drop in EKE for the entire period.

2.2. Climate Mode Indices

[8] The SAM and ENSO monthly climate mode indices are from the NOAA Climate Prediction Center Web site (http://www.esrl.noaa.gov/psd/data/climateindices/list.). The SAM index is based on geopotential height anomalies at 700 hPa in the Southern Hemisphere, while the ENSO Oceanic Niño Index is based on sea surface temperature anomalies in the Niño 3.4 region (5°N–5°S, 120–170°W) in the tropical Pacific.

2.3. Fronts

[9] The ACC is composed of a series of strong jets associated with hydrological fronts. For our study, the weekly position of the main fronts (the northern and southern branches of the Subantarctic Front (SAF-N; SAF-S) and the

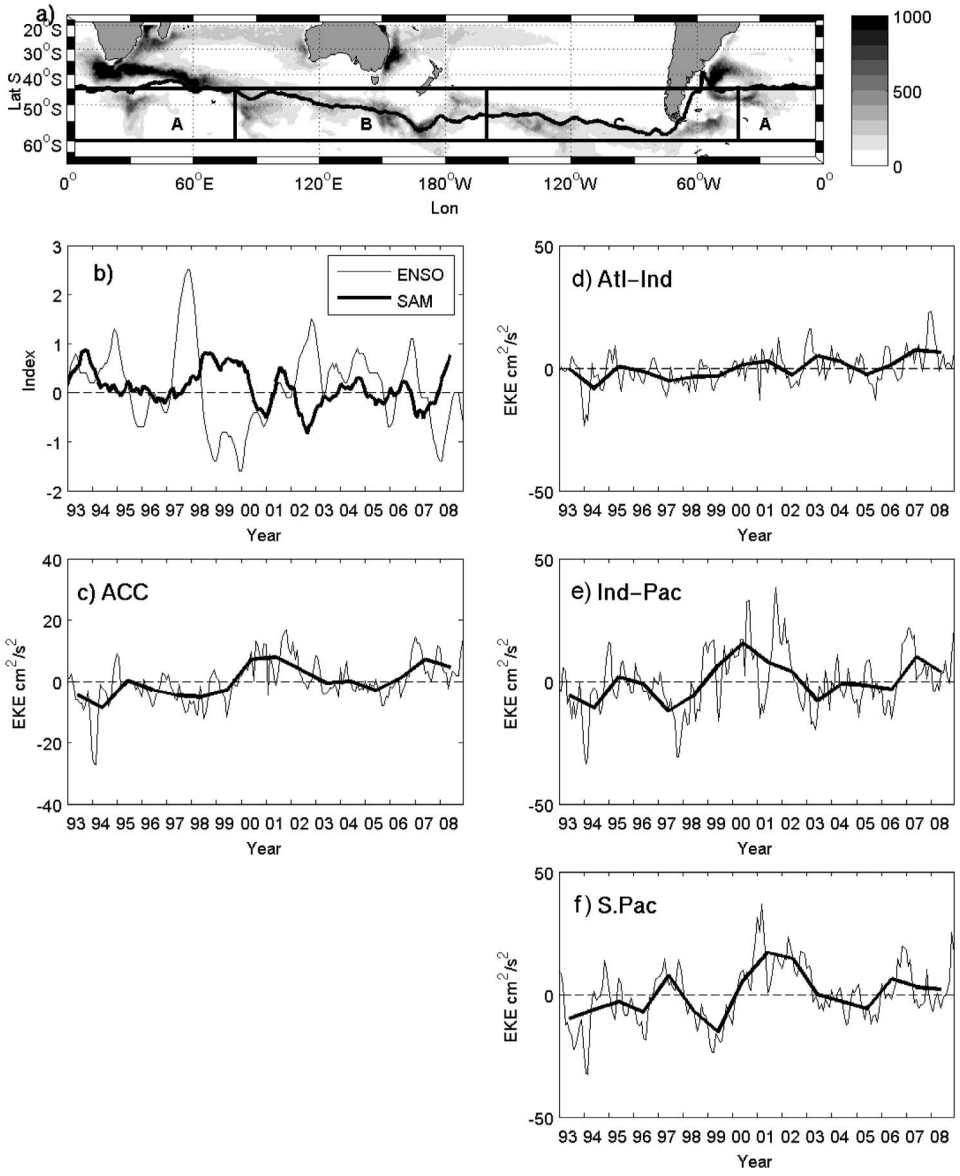

Figure 2. (a) EKE averaged over 16 years in the Southern Ocean, in $cm^2\ s^{-2}$. Black lines limit the four regions analyzed. The mean SAF-N position is contoured in black. Top left (b): Annual mean SAM (thick) and ENSO (thin) indices. Other panels show monthly (thin) and annual (thick) mean EKE from 1993 to 2009 for the five regions. Bottom left (c) ACC region, 45°S–60°S 0°E–360°E. (right) (d) Atlantic Indian section from 60°W to 60°E, (e) Indo-Pacific sector from 60°E to 180°W, (f) at the Pacific sector from 180°W to 60°W.

Polar Front (PF)) were calculated using a sea level contour which closely matches the subsurface hydrological front positions, following *Sallée et al.* [2008a] (http://ctoh.legos.obs-mip.fr/applications/mesoscale/southern-ocean-fronts).

3. Regional Variations in EKE

[10] The geographical distribution of the surface EKE in the Southern Ocean from 20°S to 65°S is shown in Figure 2a, using the 16 years of altimetric data. Long-term averages of global EKE have been analyzed previously [e.g., *Ducet et al.*, 2000]. The strongest surface EKE is associated with instabilities of the western boundary currents: the Agulhas south of Africa, the East Australian Current, and the Brazil-Malvinas Current. Along the path of the ACC, whose northern limit is delimited by the SAF-N, EKE is also enhanced with values exceeding 200 $cm^2\ s^{-2}$, except over bathymetry shallower than 3000 m where the deep-reaching eddies cannot develop. The regions in the ACC with the strongest EKE occur in deep water in close proximity to large bathymetric barriers, i.e., downstream of Kerguelen Plateau, downstream of the Southeast Indian Ridge, and Campbell Plateau, at the mid-Pacific Fracture Zone or downstream of Drake Passage.

[11] These isolated regions of high-surface EKE dominate the statistics when basin-scale averages are made, as in

MH06. In this study, we have analyzed each high EKE region separately and by basin. Figure 2b shows the monthly (thin line) and annual (thick line) variations in EKE for each of the basins highlighted in Figure 2a. The basin averages are made south of 45°S to avoid the western boundary currents. The annual average of the SAM and ENSO indices is shown for reference in Figure 2b (top left).

[12] First, although there is strong seasonal wind and heat flux forcing, including the dominant annual and semiannual oscillations [*Van Loon and Rogers*, 1983], the ocean's seasonal EKE response varies in phase and amplitude from one region to another and is modulated over time (see Figure 2b). So although the seasonal atmospheric forcing is large scale and relatively coherent around the circumpolar belt, the seasonal ocean eddy response is patchy. This may be due to a number of factors. The Southern Ocean's EKE response time is longer than the seasonal time scales (e.g., HB06), and each subbasin bounded by bathymetry will have its own spin-up response time. In addition, the bathymetry steers the ACC fronts into different latitude regimes that will be subject to different amplitudes in the seasonal forcing. In contrast to the stratified subtropics, there is little coherent seasonal response along the ACC.

[13] However, there is a clear interannual variation in the annual EKE signal in Figure 2b. When averaged over the circumpolar band, the EKE shows a 10% increase during 2000–2002, compared to its mean value (Note that the reduction in EKE in 1994 is affected by the missing ERS data during this period.). This confirms the results of MH06, who found an increase in altimetric EKE 2–3 years after the maximum peak in SAM in 1998–1999. However, although SAM has a similar amplitude during 1993, there is no EKE peak in 1995–1996. We will return to this point later. When we consider the regions of high EKE which dominate these statistics, we find a more complex response. The Indo-Pacific region peaks in 2000, dominated by the EKE south of Tasmania where there is a 20% increase in EKE from 1999 to 2002. In the South Pacific, there is a 10% decrease in EKE from the mean during 1999, followed by a 20% increase in 2001–2003. In the Atlantic-Indian basin, the interannual variations in EKE are small. All regions show a net increasing trend in EKE over the 16 year period, in keeping with the net increase in sea level in the Southern Ocean [*Lombard et al.*, 2005] and the increased trend in the SAM [*Thompson et al.*, 2000].

[14] Despite the fact that the SAM induces a coherent forcing that is in phase around the circumpolar band, the ocean's EKE response is different in each basin. In particular, the ocean EKE response is largest in the Pacific sector. The increase in EKE occurs sooner in the Indo-Pacific, and as we move toward the eastern Pacific, the peak in EKE occurs later. Why is this so?

4. Impact of SAM and ENSO on the EKE Variability

[15] SAM is not the only climate mode acting in the Pacific sector; ENSO also plays an important role. To better understand their relative impact, we have performed a lagged correlation between the monthly climate indices and the time series of EKE, taken at each point along the mean path of the SAF-N. Our SAF-N is a circumpolar streamline along the northern ACC following *Sallée et al.* [2008a] and provides a better representation of the ACC eddy response than a latitudinal average. Lagged correlations were also performed along the SAF-S and the PF (not shown); the correlations showed minor regional variations, but the large-scale patterns were the same.

[16] The lagged correlations between EKE and ENSO show a significant negative correlation in the South Pacific (Figure 3a). There is a decrease in EKE 1–2 years after a positive El Niño event and an increase in EKE 1–2 years after a La Niña event. This matches the time series of EKE in the South Pacific (Figure 2b), where EKE was minimal in 1999 after the strong El Niño of 1997/1998, and maximal in 2001–2003 following the La Niña of 1999–2000. This pattern occurs even later in the western and eastern Pacific, with EKE lagging ENSO by up to 3 years.

[17] The correlations between EKE and SAM show positive SAM events lead the increase in EKE by 2–3 years (Figure 3b), as suggested by MH06. Once again, the strongest correlations are in the Pacific sector.

[18] We have also performed lagged correlations with the two climate indices at 0–3 year intervals over the entire Southern Ocean. The significant correlation at 2 years lag are shown in Figures 3c and 3d. These figures confirm that the SAF-N does indeed pass through the regions of strong EKE and significant correlation, and that Figures 3a and 3b are representative of the larger-scale correlation patterns in each basin. Most striking is that during the analysis period (1993–2008), the lagged correlations of EKE with SAM and ENSO tend to be anticorrelated, following the anticorrelation of the indices themselves [*L'Heureux and Thompson*, 2005]. This occurs in the Southern Ocean, but also in the Indian and western Pacific subtropical gyres. The increase in EKE in the southeast Indian Ocean is strongly correlated with La Niña events [*Feng et al.*, 2003], whereas the southwest Pacific shows an increase in EKE 1 year after strong El Niño events [eg *Qiu and Chen*, 2004]. This highlights the interplay between the two climate modes, especially important in the South Pacific.

5. Comparison to Numerical Modeling

[19] Although our observations support the hypothesis that a locally variable EKE field is sensitive to wind forcing variability based on SAM and ENSO, the Southern Ocean is a dynamically complex system that is sensitive to many other influences, such as buoyancy forcing or changes to stratification by the MOC. In order to confirm that a wind-driven mechanism is sufficient to reproduce the observed EKE field, we now attempt to characterize the regional EKE response using an eddy-resolving quasi-geostrophic (QG) model (Q-GCM v1.4) [*Hogg et al.*, 2003]. Restricting ourselves to a QG framework ensures that we have a highly accurate solution of the mean current and eddy field produced solely by wind forcing and can resolve essential processes such as the eddy-saturated transport mechanism presented in HB06 and MH06. By comparing numerical QG results to observations, which potentially represent the complete dynamics of the Southern Ocean, we can determine whether the observed EKE field can be explained by QG dynamics and eddy saturation theory.

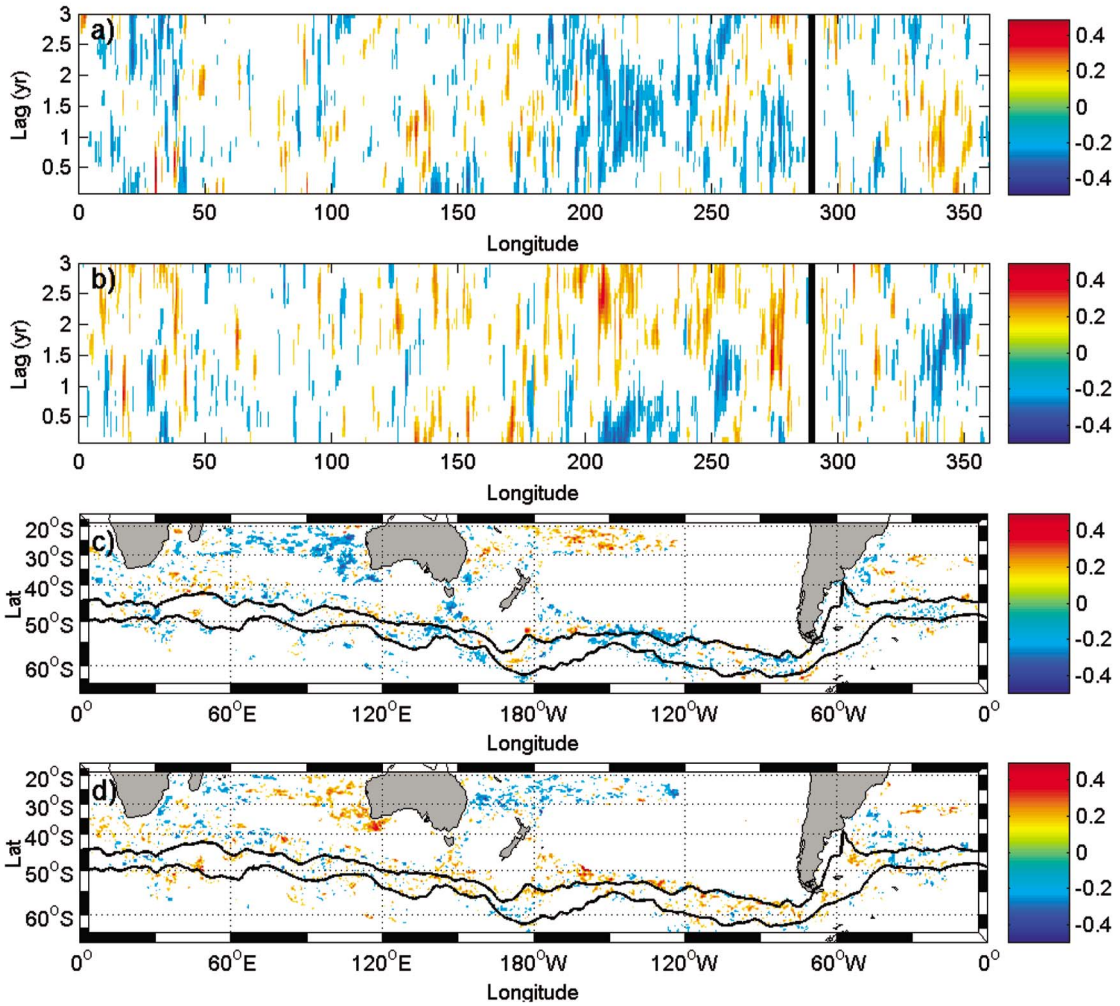

Figure 3. Lagged correlations between the monthly EKE time series and (a) ENSO and (b) SAM indices, for each point in longitude along the mean position of the SAF-N (x axis). Lags range from 0 to 3 years (y axis). Drake Passage is marked by the black vertical line. Spatial distribution of the 2 year lagged correlation from monthly EKE with (c) ENSO and (d) SAM indices. The thin black contour lines show the SAF-N and the PF, after *Sallée et al.* [2008a]. Only EKE values > 80 cm^2 s^{-2} and significant at the 95% level are shown.

[20] We use the ocean-only implementation of Q-GCM as described in HB06, where the atmospheric component of the coupled QG model is replaced by a prescribed surface wind forcing (detailed below). The model simulates three quasi-geostrophic ocean layers with thicknesses of 300, 1100, and 2600 m, respectively, and with internal gravity accelerations of 5×10^{-2} and 2.5×10^{-2} m s^{-2} for the upper and lower interfaces. The model is run at a high resolution ($\Delta x = 10$ km) relative to the largest deformation radius ($r_d = 33$ km) and uses a low biharmonic viscosity ($A_4 = 10^{10}$ m^4 s^{-1}), ensuring that there is a well-resolved eddy field. Our simulations are exclusively wind driven, and any response is due solely to the resulting Ekman pumping. As in HB06, the Southern Ocean has been modeled as a zonally reentrant channel. The channel is 23,040 km × 2880 km, with partial-slip walls along the northern and southern boundaries [*Haidvogel et al.*, 1992] and a bathymetry derived from the data set of *Smith and Sandwell* [1997]. In order to constrain large variations of bathymetry, which would violate the underlying assumptions of QG theory, depths that are either 900 m above and below the mean depth ($D = 4000$ m) have been truncated. As a result, the bathymetry remains within the bottom layer, and large regions of the model contain flat plateaus of 900 m height, relative to the bottom depth (see Figure 7c). Detailed coastlines have been replaced by zonal boundaries, and defining features such as a narrow Drake Passage have been removed. While it is unlikely that such a bathymetry could accurately reproduce global quantities such as the net ACC transport, the general topographic structure of the Southern Ocean, such as major basins and ridges, is still preserved and provides a reasonable representation of the local conditions of Southern Ocean EKE sensitivity to forcing.

[21] The applied atmospheric pressure fields are based on the NOAA Climate Prediction Center data presented in the previous section and are shown in Figure 4, and the associated wind stress magnitudes are shown in Figure 5. Strong pressure gradients due to coastal temperature differences were removed by Laplacian smoothing, since our model does not

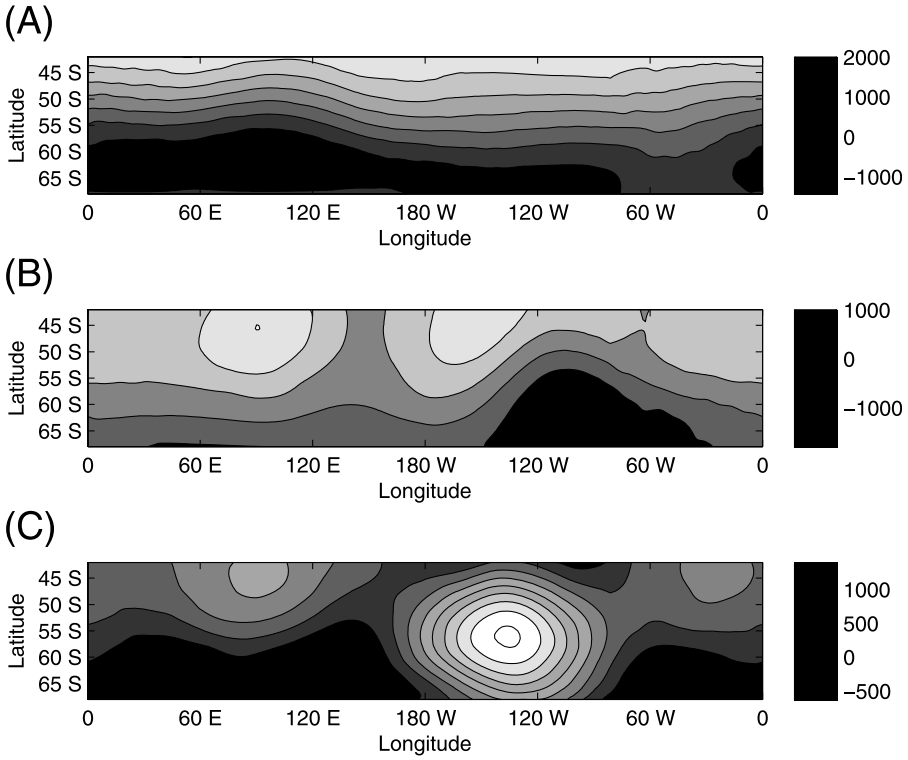

Figure 4. Spatial maps of kinematic pressure fields P/ρ (for pressure P and mean density ρ) for (a) the mean state and the (b) SAM and (c) ENSO modes.

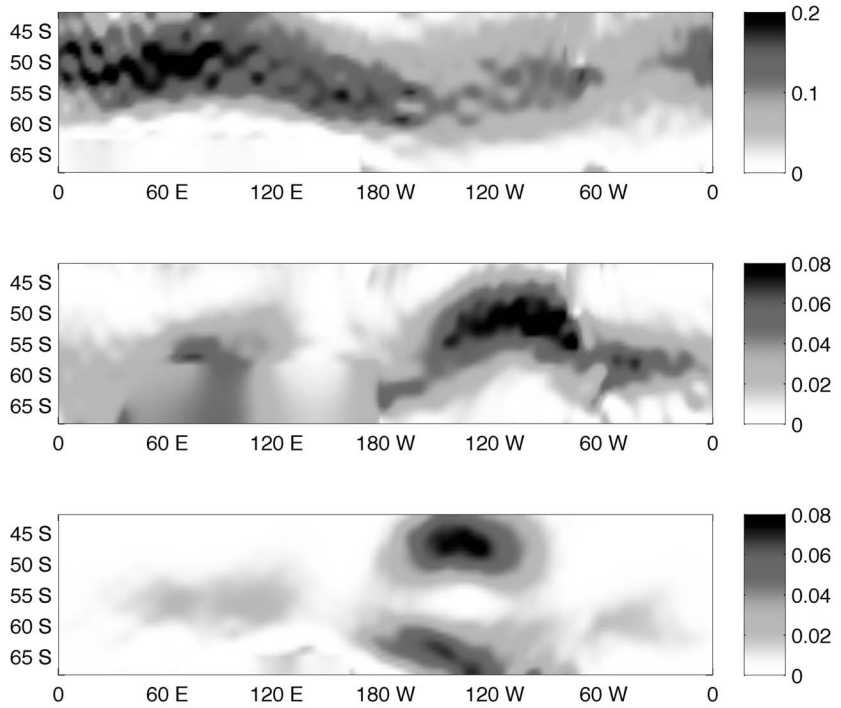

Figure 5. Spatial maps of geostrophic wind stress magnitude due to the pressure fields in Figure 4. Sharp pressure gradients due to land-sea temperature differences have been removed by Laplacian smoothing, producing regions of zero Ekman pumping.

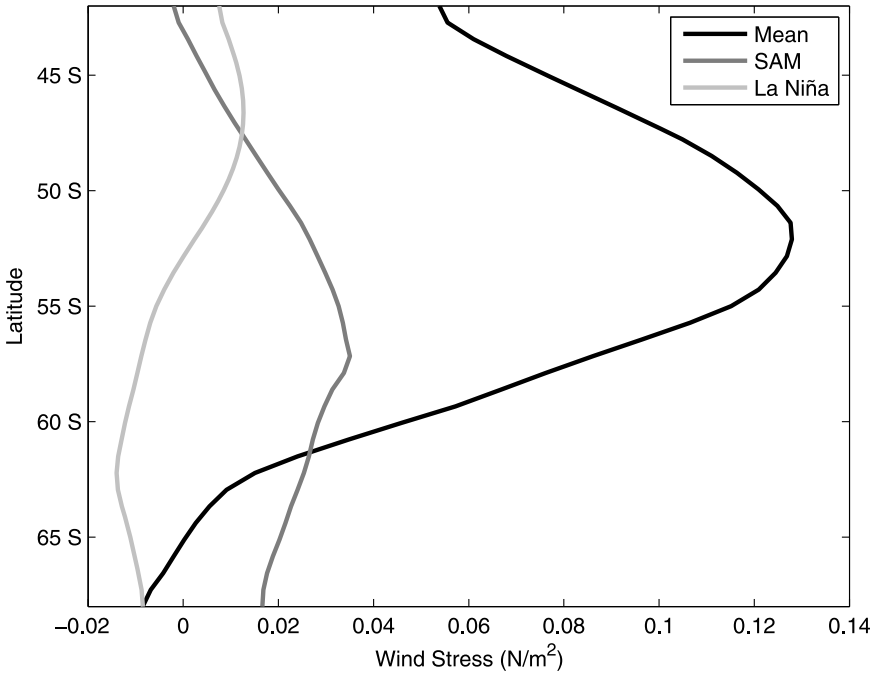

Figure 6. Zonally averaged wind stress used in the model due to the mean pressure field and the SAM and ENSO EOFs.

contain realistic coastlines, which replaces these regions with patches of zero wind stress curl and eliminates any anomalous Ekman pumping. The wind stress field τ was determined from a quadratic drag law of the form $\tau = \rho_a C_d |\mathbf{u}|\mathbf{u}$, where ρ_a is the atmospheric density and the velocities $\mathbf{u}$ are derived from the geostrophic velocities induced by the atmospheric pressure. The drag coefficient C_d was chosen to be 0.7×10^{-3}; this is lower than more traditional values closer to 1.3×10^{-3}, but it ensures that our wind stresses are within an observed range of about $|\tau| \leq 0.18$ N m^{-2} [*Josey et al.*, 2002]. Zonally averaged wind stress profiles due to the mean state and each EOF are shown in Figure 6.

[22] The model ocean was continuously forced by the mean pressure field (Figure 4a), which was also used during spin-up to define an equilibrium state. In the spirit of MH06, a time-dependent wind stress due to the SAM (Figure 4b) and ENSO (Figure 4c) EOFs is temporarily applied atop this forcing, and the EKE response is observed. The temporal forcing is a half-sinusoidal pulse that reaches its maximum amplitude after one year and is terminated after two years. Our results are ensemble averages based on twenty independent simulations, where each initial condition is sampled from the equilibrium state. This allows us to consider many different combinations of applied EOF forcings and to independently assess the impact of each mode. The model kinetic energy output is reported in units of J m^{-2} rather than cm^2 s^{-2}, since the model is based on layered dynamics rather than direct velocity measurements, but both quantities are reliable indicators of the regional EKE response.

[23] The time-averaged EKE distribution due to the mean pressure field, shown in Figure 7, broadly resembles the observational distribution. Both identify three major areas of EKE activity: a sharp, localized region downstream of Kerguelen plateau (100°E), a broad zone of activity south of Australia, from the Indian-Antarctic Ridge to Campbell Plateau (150°E–180°W), and a weaker regional response in the South Pacific basin (120°W–80°W). The observed region of strong EKE activity downstream of the Drake Passage is not present in our model, since this is not a resolved topographic feature. The model topography is shown in Figure 7c.

[24] The channel-averaged responses to different SAM and ENSO forcings are shown in Figure 8. As in MH06, the EKE response to SAM in Figure 8a produces a strong, coherent peak about 2 years after the time of maximum forcing, after which there is a gradual return to the equilibrium state due to wind forcing from the mean pressure field. Additionally, the relationship between the EOF-induced wind forcing and EKE response is approximately linear in nature: a doubling of the wind stress yields a doubling of the EKE, while a reversal of the SAM mode phase (which should reduce winds relative to the mean state) produces a reduction in average EKE. In contrast, ENSO forcing produces no measurable circumpolar-averaged EKE response, as demonstrated by the absence of any coherent peak in Figure 8b.

[25] A regional analysis reveals a more subtle picture. Hovmöller diagrams of the latitude-averaged response over time (Figure 9) show that the major regions of EKE activity are individually sensitive to wind forcing, but to varying degrees. The EKE anomaly is presented as the difference in latitude-averaged EKE of the mean state and the EOF-forced response. Figure 9a shows that the Pacific basin is the most sensitive to SAM forcing, despite the comparatively low level of EKE activity. The Atlantic-Indian basin is less sensitive but still yields a coherent response. The regions downstream of Kerguelen peninsula and south of Australia reveal strong and more locally concentrated responses. Additionally, each region has a different response time, showing that the lagged response time of the circumpolar-averaged

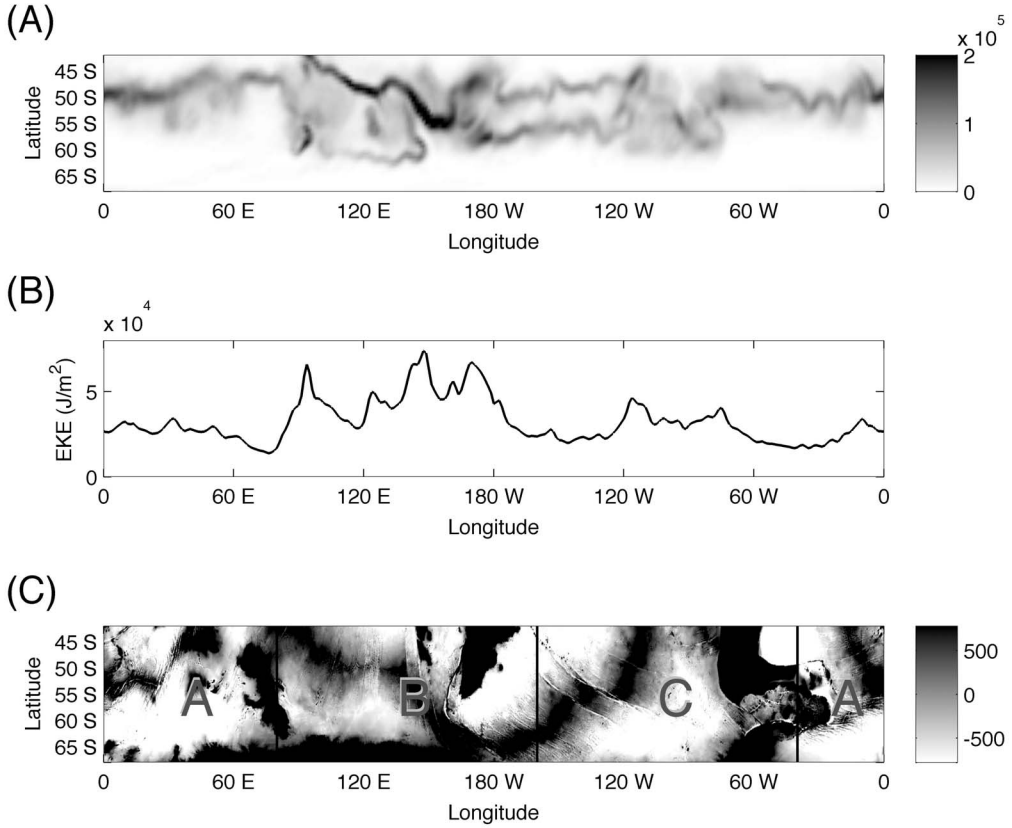

Figure 7. (a) Mean EKE distribution of the model in the top layer. (b) Latitudinally averaged EKE. These results are used to define three major zones of EKE activity: (a) the Atlantic-Indian Basin, (b) south of Australia, and (c) the Pacific Basin, denoted on the topographic map.

EKE peaks in Figure 8 may represent an average response over several basins, rather than a single coherent time scale.

[26] The regional ENSO response, shown in Figure 9b, is less uniform. During a La Niña period (or a negative ENSO mode), the Pacific basin exhibits increased EKE activity, while the Atlantic and Indian EKE becomes reduced. During an El Niño period, these trends are reversed. Although this produces no net change in EKE across the channel, it shows that the ENSO mode is capable of altering the local EKE distribution.

[27] To quantify these responses in more detail, basin-wide averages are shown in Figure 10. We average over each of the three regions outlined in the topographic map (Figure 7c) and consider the response of each mode, as well as the SAM response during both an El Niño and a La Niña event. As in the Hovmöller diagrams, each region is excited by the SAM mode. But the impact of ENSO on each basin is more coherent in the regional averages: SAM is amplified during La Niña, and suppressed by El Niño in the Pacific basin (Figure 10c), while the reverse is true in the Atlantic-Indian basin (Figure 10a). There is strong variability near Kerguelen and south of Australia, but the integrated response shows that ENSO has no net effect over these regions.

[28] This response is consistent with our profiles of wind stress in Figure 5, where both EOFs produce elevated energy input across the Pacific basins near 120°W, and to a lesser extent across the Atlantic-Indian Basin near 80°E, although this does not take topographic constraints into account. To confirm that the energetic response remains local, we look at the quasi-geostrophic energy flux vector [*Pedlosky*, 1987], which for each layer k is given by

$$S^k = -\frac{\rho H^k}{f_0} p^k q^k u^k - \frac{\rho H^k}{f_0^2} p^k \nabla\left(\frac{\partial p^k}{\partial t}\right)$$

for background density ρ, mean layer depth H^k, Coriolis parameter f_0, pressure field p^k, potential vorticity q^k, and geostrophic velocities u^k. If we sum over all layers, then $S = \sum S^k$ describes the lateral transport of energy produced by Ekman pumping, bottom friction, and numerical viscosity. This energy transfer is quantified in Figure 11, which shows $\int |S_x| dy$, the latitudinal integral of zonal energy flux, for each longitude over time. Since we are summing the absolute value of S_x, it is not a true measure of net energy flux across a particular longitude, but rather a measure of "flux activity," so that low values on Figure 11 represent reduced rates of energy flux. In all of the figures, the largest values are restricted to localized bands, such as near 180°W, suggesting that the eddy-saturated response due to wind forcing is generally a localized effect. These bands of high zonal energy flux correspond to the subbasins with higher EKE in Figure 7. Elevated responses in the Pacific (120°W, 60°W) due to SAM and La Niña also remain highly localized, as do weaker responses in the Atlantic-Indian basin (30°E). Of

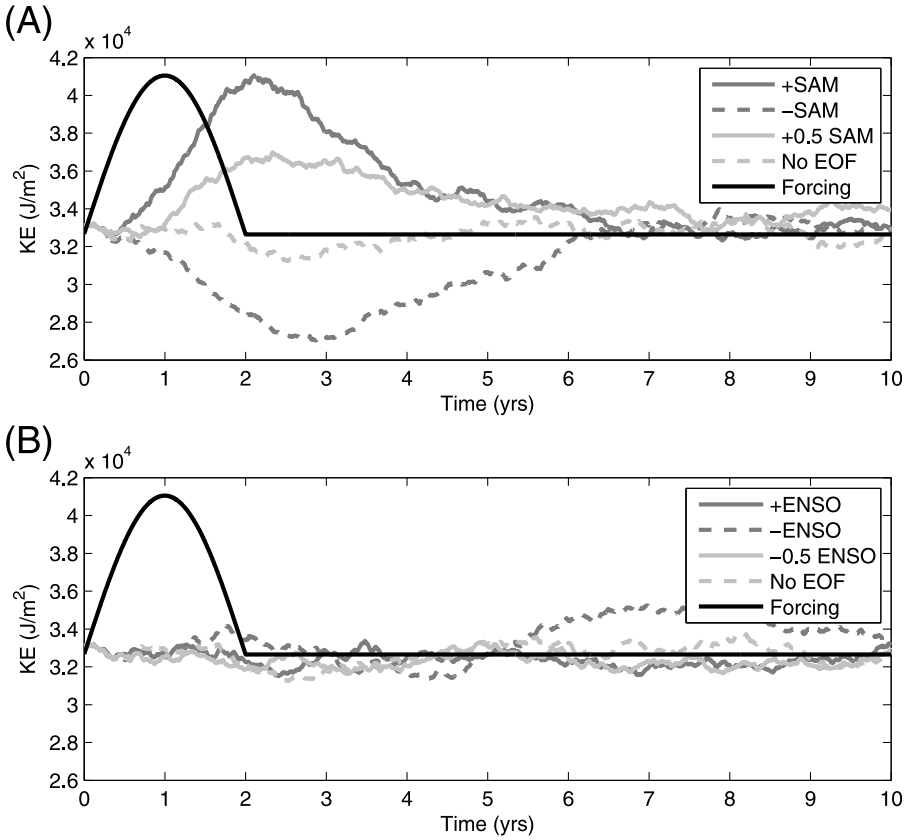

Figure 8. Channel averaged EKE response due to (a) SAM and (b) ENSO modes. The black line denotes the qualitative structure of the pulse forcing, while the other lines denote a response to a SAM pulse (dark gray), a half-strength pulse (light gray), and a reverse-sign SAM (dark dashed), along with the unforced state (light dashed). A positive/negative ENSO mode corresponds to an El Niño/La Niña phase.

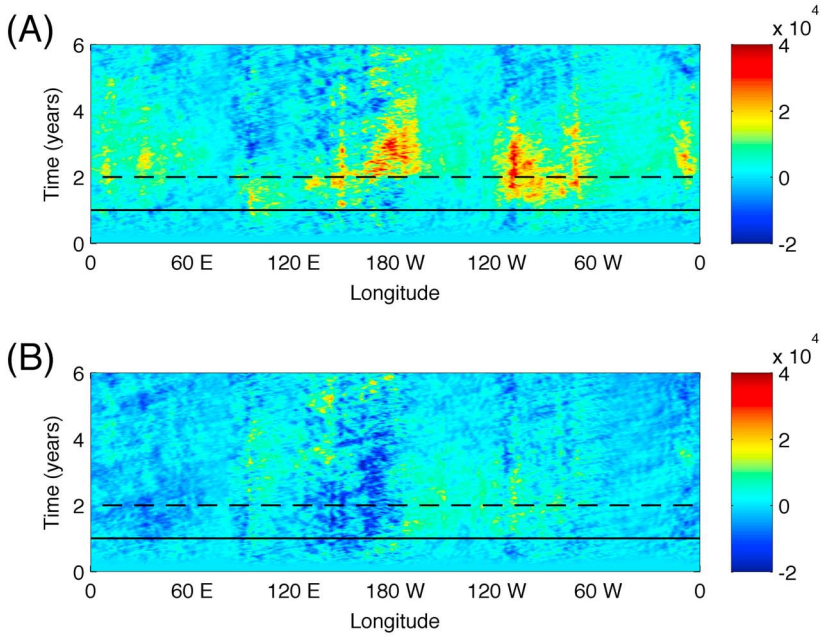

Figure 9. Hovmöller plot of the latitude-averaged EKE response due to (a) SAM and (b) La Niña. The EKE anomaly is shown, defined as relative to the equilibrium state. The solid black line denotes the forcing peak, and forcing ceases after the dashed black line.

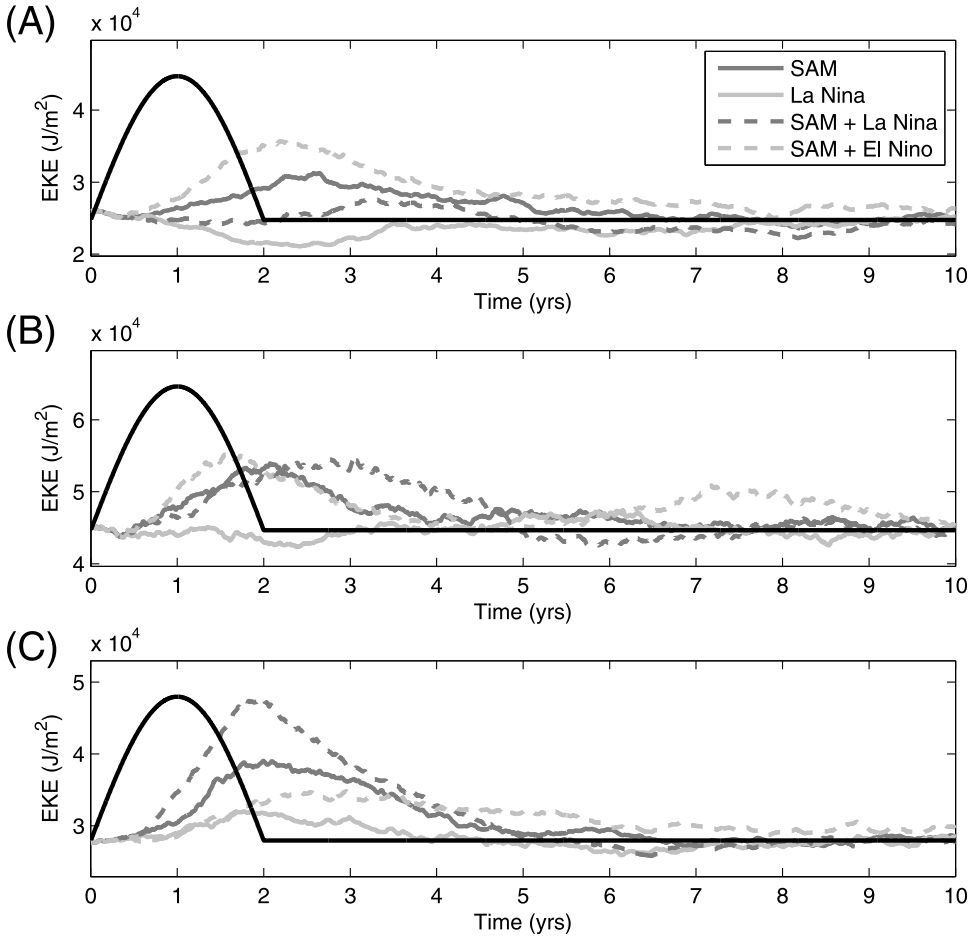

Figure 10. Basin-averaged responses based on the regions defined in Figure 7c; (a) the Atlantic-Indian basin, (b) the basins south of Australia, and (c) the Pacific basin.

particular note is the presence of "dead zones" at approximately 70°E and 30°W, as well as 150°W to a lesser extent, where the net latitudinal energy flux drops by an order of magnitude. The absence of any major energy flux activity across these latitudes suggests that the currents of the Pacific and Atlantic-Indian basins remain energetically isolated with respect to wind forcing and their eddy response, and support the assertion that the eddy-saturated mechanism of MH06 for channel-averaged flows can also be applied on a regional basis.

6. Discussion

[29] Our study confirms the results of MH06, that basin-scale averages of EKE do show an increase 2–3 years after the strong SAM event in 1998–1999, with the strongest response in the Pacific sector. A more detailed analysis has revealed strong regional differences in the phase and amplitude of the EKE response, despite the fact that SAM is an annular mode and the wind forcing is in phase right around the circumpolar belt. So why is the response so strong in the Pacific sector, and why does the SAM event of 1993 have such a weak EKE response?

[30] We propose that the EKE response is particularly strong after the 1998–99 SAM event because it coincided with a strong La Niña period. During La Niña (negative ENSO index), the spatial pattern of SLP and surface winds is the reverse of Figure 1b, which enhances the effects of the positive SAM forcing described above. When a strong positive SAM event coincides with an El Niño period (positive ENSO index), as occurs in 1993, the SLP and surface winds are in opposition to the SAM forcing, leading to a much weaker forcing and ocean EKE response.

[31] Numerical modeling supports this hypothesis. When the model is forced with both SAM and ENSO modes simultaneously, the Ekman pumping due to each mode is in phase, so that the EKE response in the South Pacific region is enhanced by La Niña and damped by ENSO. The reverse applies in the South Atlantic where El Niño amplifies the local EKE in the model. The absence of any substantial energy flux between these basins confirms that these are independent, localized responses. There are some discrepancies between the observations and modeling. For example, ENSO forcing alone does not alter circumpolar mean EKE in our modeling results nor does it modify the circumpolar response to SAM. We attribute this primarily to the model response in the Atlantic-Indian basin; the model response in this region acts in opposition to the Pacific, where observations show a negligible response to both modes (most likely because of the absence of coastlines and a Drake Passage in the model). Nonetheless, we argue that the principal result, which can be drawn from both model and observations, is

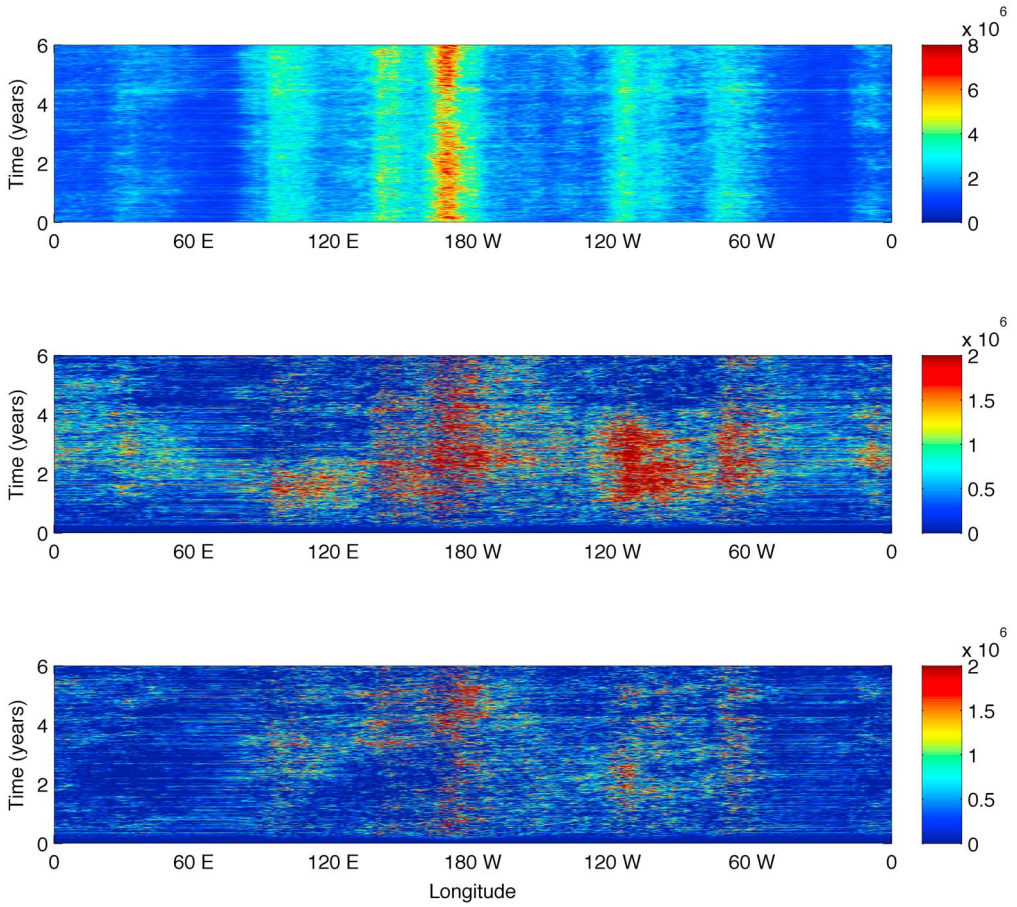

Figure 11. Hovmöller plots of the integrated zonal energy flux vector, $\int |S_x| dy$, for each longitude over time. (top) Zonal energy flux due to the mean forcing. (middle and bottom) The difference of zonal energy flux due to the climate mode forcing, with respect to the mean forcing energy flux. (middle) Anomaly due to SAM; (bottom) anomaly due to La Niña.

that basin-scale variations in wind stress forcing alter the local (i.e., basin scale) eddy field.

[32] This result is significant for several reasons. First, it implies that if the eddy saturation hypothesis holds, then it may hold on local scales as well as circumpolar scales. It is not immediately obvious that such localization should occur, since potential energy anomalies (which are the first response to wind stress forcing) are capable of propagating to another part of the domain before becoming unstable and contributing energy to the eddy field. The present results show that instability occurs faster than propagation. Second, previous studies have implied that increases in EKE will facilitate meridional heat transport [*Hogg et al.*, 2008; *Sallée et al.*, 2008b]. Strong regional variations in the EKE distribution and in sensitivity to wind forcing may yield similar variability in heat transport, which can have broader implications for global climate.

[33] The numerical modeling also shows that the highest EKE regions do not always produce the greatest EKE sensitivity. In general, we found that the EKE response at any location depended upon the size of the local wind stress forcing anomaly, the specific details of the local topography, and the preexisting mean flow state at that location.

[34] Finally, the MH06 model (and the one used for the present paper) is based on a "saturated" ocean field, where additional wind forcing leads to an increase in the EKE rather than in the mean flow. To verify this, we have checked the transport of the ACC south of Tasmania, estimated from a combination of in situ and altimetric observations [*Rintoul et al.*, 2002] now made available over the entire altimetric period (S. Sokolov, personal communication). The ACC transport increases by only 5% during the period 1998–2003 with a peak in 2000, close to the so-called "saturated" state.

7. Conclusions

[35] A circumpolar analysis of altimetric data has been used to investigate the evolving EKE field in the Southern Ocean. When large-scale averaging is performed along the circumpolar belt, we indeed find a peak in EKE from 2000 to 2002, 2–3 years after the peak in the SAM index, as reported by MH06. However, this EKE signal is dominated by specific regions with high EKE near major bathymetric features. A regional analysis of these high EKE zones reveals a more complex structure, with no clear peak in the southern Indian Ocean, but a strong EKE signal in the Pacific, occurring

progressively later toward the east. Despite the fact that SAM is an annular mode, and its forcing is in phase around the circumpolar band, we find the oceanic EKE response varies from one region to another.

[36] We suggest that the stronger EKE response in the Pacific sector is due to the presence of two climate modes, SAM and ENSO. When strong positive SAM events coincide with La Niña (negative ENSO) events, as happened in 1999, anomalous meridional wind forcing is enhanced in the South Pacific Ocean, inducing the observed increase in EKE 2–3 years later. However, when positive SAM events coincide with El Niño events, as in 1993, the climate modes are in opposition in the South Pacific, which could explain the weak EKE response during the mid 1990s.

[37] This explanation has been confirmed using an eddy-resolving model of the Southern Ocean. When a wind stress pulse based on the SAM EOF is applied to the model, the EKE response is isolated to specific regions, with the strongest response in the Pacific. When the ENSO winds are added to this signal, there is a reduced Pacific EKE response during El Niño and an increased response during La Niña, which is consistent with observations. More broadly, we can infer that the EKE depends on local interactions between wind stress, topography, and mean state.

[38] The relation between the evolution of these large-scale climate modes, and the local EKE response, is important for the Southern Ocean heat, salt, and carbon budgets. In energetic regions, varying EKE levels will have a direct impact on the eddy diffusion of these tracers [*Sallée et al.*, 2008c]. This could introduce interannual variations in the poleward heat and salt transports in these regions, which then dominate the circumpolar averages of these budgets. Local variations in EKE and eddy diffusion also modify the volume and water mass characteristics of mode waters formed north of the ACC [*Sallée et al.*, 2008b].

[39] **Acknowledgments.** M.L.W. and A.M.H. were supported by Australian ARC Discovery Project DP0877824, and R.M. and S.P. were supported by the French TOSCA program. Numerical computations were supported by the Australian National Facility of the National Computational Infrastructure.

References

Ducet, N., P. Le Traon, and G. Reverdin (2000), Global high-resolution mapping of ocean circulation from TOPEX/Poseidon and ERS-1 and -2, *J. Geophys. Res.*, *105*, 19,477–19,498, doi:10.1029/2000JC900063.

Feng, M., G. Meyers, A. Pearce, and S. Wijffels (2003), Annual and interannual variations of the Leeuwin Current at 32°S, *J. Geophys. Res.*, *108* (C11), 3355, doi:10.1029/2002JC001763.

Haidvogel, D. B., J. C. McWilliams, and P. R. Gent (1992), Boundary current separation in a quasi-geostrophic, eddy-resolving ocean circulation model, *J. Phys. Oceanogr.*, *22*, 882–902.

Hogg, A. M., and J. R. Blundell (2006), Interdecadal variability of the Southern Ocean, *J. Phys. Oceanogr.*, *36*, 1626–1644.

Hogg, A. M., W. K. Dewar, P. D. Killworth, and J. R. Blundell (2003), A quasi-geostrophic coupled model: Q-GCM, *Mon. Weather Rev.*, *131*(10), 2261–2278.

Hogg, A. M., M. P. Meredith, J. R. Blundell, and C. Wilson (2008), Eddy heat flux in the Southern Ocean: Response to variable wind forcing, *J. Clim.*, *21*, 608–620.

Johnson, G. C., and H. C. Bryden (1989), On the size of the Antarctic Circumpolar Current, *Deep-Sea Res.*, *36*, 39–53.

Josey, S. A., E. C. Kent, and P. K. Taylor (2002), On the wind stress forcing of the ocean in the SOC climatology: Comparisons with the NCEP/NCAR, ECMWF, UWM/COADS, and Hellerman and Rosenstein data sets, *J. Phys. Oceanogr.*, *32*(7), 1993–2019.

Karoly, D. (1989), Southern Hemisphere circulation features associated with El Nino-Southern Oscillation events, *J. Clim.*, *2*, 1239–1252.

L'Heureux, M., and D. Thompson (2005), Observed relationships between the El Niño-Southern Oscillation and the extratropical zonal-mean circulation, *J. Clim.*, *19*, 276–287.

Lombard, A., A. Cazenave, P. Y. Le Traon, and M. Ishii (2005), Contribution of thermal expansion to present-day sea level change revisited, *Global Planet. Change*, *47*, 1–16.

Meredith, M. P., and A. M. Hogg (2006), Circumpolar response of Southern Ocean eddy activity to changes in the Southern Annular Mode, *Geophys. Res. Lett.*, *33*, L16608, doi:10.1029/2006GL026499.

Munk, W. H., and E. Palmén (1951), Note on the dynamics of the Antarctic Circumpolar Current, *Tellus*, *3*, 53–55.

Pedlosky, J. (1987), *Geophysical Fluid Dynamics*, 2nd ed., 710 pp., Springer, New York.

Qiu, B., and S. Chen (2004), Seasonal modulations in the eddy field of the South Pacific Ocean, *J. Phys. Oceanogr.*, *34*, 1515–1527.

Rintoul, S. R., S. Sokolov, and J. Church (2002), A 6 year record of baroclinic transport variability of the Antarctic Circumpolar Current at 140°E derived from expendable bathythermograph and altimeter measurements, *J. Geophys. Res.*, *107*(C10), 3155, doi:10.1029/2001JC000787.

Sallée, J. B., R. Morrow, and K. Speer (2008a), Southern Ocean fronts and their variability to climate modes, *J. Clim.*, *21*, 3020–3039.

Sallée, J. B., R. Morrow, and K. Speer (2008b), Eddy heat diffusion and Subantarctic Mode Water formation, *Geophys. Res. Lett.*, *35*, L05607, doi:10.1029/2007GL032827.

Sallée, J. B., R. Morrow, K. Speer, and R. Lumpkin (2008c), An estimate of Lagrangian eddy statistics and diffusion in the mixed layer of the Southern Ocean, *J. Mar. Res.*, *66*, 441–463.

Smith, W. H. F., and D. T. Sandwell (1997), Global seafloor topography from satellite altimetry and ship depth soundings, *Science*, *277*, 1957–1962.

Stammerjohn, S. E., D. G. Martinson, R. C. Smith, X. Yuan, and D. Rind (2008), Trends in Antarctic annual sea ice retreat and advance and their relation to ENSO and SAM variability, *J. Geophys. Res.*, *113*, C03S90, doi:10.1029/2007JC004269.

Thompson, D., and J. Wallace (2000), Annular mode in the extratropical circulation: Part I. Month-to-Month Variability, *J. Clim.*, *13*, 1000–1016.

Thompson, D. C., J. Wallace, and G. C. Hegerl (2000), Annular modes in the extratropical circulation: Part II. Trends, *J. Clim.*, *13*, 1018–1036.

Treguier, A. M., M. H. England, S. R. Rintoul, G. Madec, J. Le Sommer, and J.-M. Molines (2007), Southern Ocean overturning across streamlines in an eddying simulation of the Antarctic Circumpolar Current, *Ocean Sci.*, *3*, 491–507.

Van Loon, H., and J. C. Rogers (1983), The yearly wave in pressure and zonal geostrophic wind at sea level on the Southern Hemisphere and its interannual variability, *Tellus A*, *36*, 348–354.

R. Morrow and S. Pasquet, LEGOS/CNRS, 18 avenue Edouard Belin, 31401 Toulouse, France. (Rosemary.Morrow@legos.obs-mip.fr)

A. M. Hogg and M. L. Ward, Research School of Earth Sciences, Australian National University, Canberra ACT 0200, Australia.